FULL PAPER

Magnetic Resonance in Medicine 00:00–00 (2017)

Temporally Resolved Parametric Assessment of Z-Magnetization Recovery (TOPAZ): Dynamic Myocardial T_1 Mapping Using a Cine Steady-State Look-Locker Approach

Sebastian Weingärtner,[1,2,3] Chetan Shenoy,[4] Benedikt Rieger,[3] Lothar R. Schad,[3] Jeanette Schulz-Menger,[5,6] and Mehmet Akçakaya[1,2]

Purpose: To develop and evaluate a cardiac phase-resolved myocardial T_1 mapping sequence.

Methods: The proposed method for temporally resolved parametric assessment of Z-magnetization recovery (TOPAZ) is based on contiguous fast low-angle shot imaging readout after magnetization inversion from the pulsed steady state. Thereby, segmented k-space data are acquired over multiple heartbeats, before reaching steady state. This results in sampling of the inversion-recovery curve for each heart phase at multiple points separated by an R-R interval. Joint T_1 and B_1^+ estimation is performed for reconstruction of cardiac phase-resolved T_1 and B_1^+ maps. Sequence parameters are optimized using numerical simulations. Phantom and in vivo imaging are performed to compare the proposed sequence to a spin-echo reference and saturation pulse prepared heart rate–independent inversion-recovery (SAPPHIRE) T_1 mapping sequence in terms of accuracy and precision.

Results: In phantom, TOPAZ T_1 values with integrated B_1^+ correction are in good agreement with spin-echo T_1 values (normalized root mean square error = 4.2%) and consistent across the cardiac cycle (coefficient of variation = $1.4 \pm 0.78\%$) and different heart rates (coefficient of variation = $1.2 \pm 1.9\%$). In vivo imaging shows no significant difference in TOPAZ T_1 times between the cardiac phases (analysis of variance: $P = 0.14$, coefficient of variation = $3.2 \pm 0.8\%$), but underestimation compared with SAPPHIRE (T_1 time $\pm$ precision: 1431 ± 56 ms versus 1569 ± 65 ms). In vivo precision is comparable to SAPPHIRE T_1 mapping until middiastole ($P > 0.07$), but deteriorates in the later phases.

Conclusions: The proposed sequence allows cardiac phase-resolved T_1 mapping with integrated B_1^+ assessment at a temporal resolution of 40 ms. **Magn Reson Med 000:000–000, 2017. © 2017 International Society for Magnetic Resonance in Medicine.**

Key words: quantitative myocardial tissue characterization; T_1 mapping; B_1^+ mapping; cine; cardiac imaging

INTRODUCTION

Cardiovascular MRI has a major role in the diagnosis, staging, and monitoring of numerous ischemic and nonischemic cardiomyopathies (1–3). Recently, parameter mapping in the heart has expanded the cardiovascular MRI toolbox, offering the chance to detect diffuse pathologies and to perform quantitative diagnosis. Among the quantitative imaging technologies, myocardial T_1 mapping has shown promising diagnostic and prognostic value in a wide range of diseases (4–7).

Early techniques for the quantification of the longitudinal relaxation time (T_1) in the heart have used continuous imaging using equidistant fast low-angle shot (FLASH) excitations, following an initial inversion pulse, as originally proposed by Look and Locker (8). Although such approaches did not provide a pixel-wise T_1 map due to the absence of electrocardiographic (ECG) triggering, they allowed for a regional estimation of myocardial T_1 using a region of interest (ROI) analysis (9). For voxel-wise quantification, the modified Look-Locker inversion-recovery sequence was introduced, performing single-shot imaging, triggered to the end-diastolic quiescence in a Look-Locker-type inversion-recovery experiment (10). This enabled spatially resolved quantification of the T_1 time as a parameter map (T_1 mapping) and established widespread use of quantitative cardiovascular MRI. Other imaging sequences, based on inversion (11–13) or saturation (14,15) recovery or a combination of both (16,17), have been subsequently introduced for myocardial T_1 mapping, each offering a distinct profile of advantages and disadvantages (18–20).

Myocardial T_1 maps are conventionally acquired at a single end-diastolic phase. Recently, quantitative imaging during systole has been introduced, promising reduced effects of partial voluming (21), as well as increased resilience to heart-rate variability (22). In addition, imaging throughout the cardiac cycle using variable flip angle (FA) steady-state acquisitions has been explored for quantitative

[1]Electrical and Computer Engineering, University of Minnesota, Minneapolis, Minnesota, USA.

[2]Center for Magnetic Resonance Research, University of Minnesota, Minneapolis, Minnesota, USA.

[3]Computer Assisted Clinical Medicine, University Medical Center Mannheim, Heidelberg University, Mannheim, Germany.

[4]Cardiovascular Division, Department of Medicine, University of Minnesota, Minneapolis, Minnesota, USA.

[5]Working Group on Cardiovascular Magnetic Resonance Imaging, Experimental and Clinical Research Center, Joint Cooperation of the Max-Delbrück-Centrum and Charité-Medical University Berlin, Berlin, Germany.

[6]Department of Cardiology and Nephrology, HELIOS Klinikum Berlin-Buch, Berlin, Germany.

Grant Support: NIH, grant numbers R00HL111410 and P41EB015894; NSF, grant number CCF-1651825.

S.W. and M.A. are inventors of an US and European patent describing the SAPPHIRE sequence.

*Correspondence to: Sebastian Weingärtner, Ph.D., Electrical and Computer Engineering, University of Minnesota, 200 Union Street SE, Minneapolis, MN 55455, USA. E-mail: sweingae@umn.edu.

Received 29 January 2017; revised 2 August 2017; accepted 2 August 2017

DOI 10.1002/mrm.26887

Published online 00 Month 2017 in Wiley Online Library (wileyonlinelibrary.com).

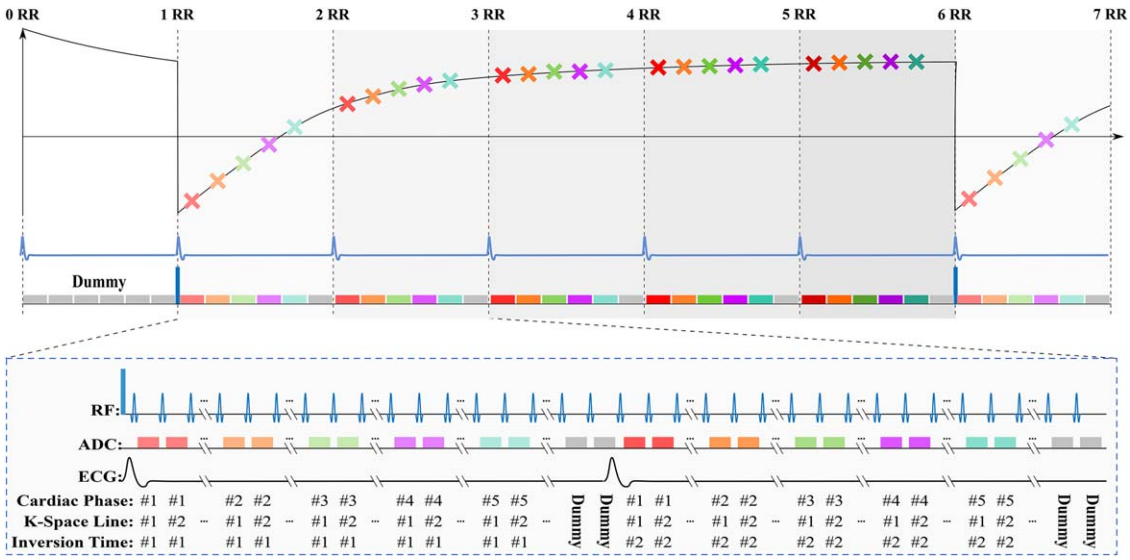

FIG. 1. Sequence diagram of the proposed TOPAZ T_1 mapping acquisition. The signal is first driven to steady state using continuous FLASH excitations. After an initial magnetization inversion, FLASH pulses are continuously played to allow for the sampling of an apparent T_1 relaxation curve. k-Space readouts are segmented across several heart phases for sufficient temporal resolution. Multiple inversion times are sampled on the inversion-recovery curve until pulsed steady state is reached and another magnetization inversion is performed, after five R-R intervals in the diagram, to sample the next k-space segment. This is repeated several times to fill the k-space for each cardiac phase at five different inversion times.

mapping in a preclinical mouse study (23). However, due to limitations of the B_1^+ correction in the sequence, quantitative T_1 times were only derived at the end-diastolic phase.

Quantitative analysis of the T_1 time in the myocardium conventionally entails manually delineating the myocardium from the surrounding blood pools. Hence, consistent contouring of the myocardium is paramount for the reproducibility of cardiac T_1 measurements (19,24). However, subepicardial fat, fatty infiltrations, myocardial crypts, trabeculae, and other structures have previously been shown to hamper the identification of the blood myocardial interface in single-phase cardiac images (25). Furthermore, wall motion abnormalities, including asynchrony patterns caused by bundle branch blocks, are challenging in diastolic imaging and are commonly observed in cardiac diseases. Superior temporal resolution or the ability to view the changes in these structures over the cardiac phase may facilitate differentiation.

In this study, we sought to develop a method that allows for temporally and spatially resolved mapping of the native myocardial T_1 times. The proposed sequence for temporally resolved parametric assessment of Z-magnetization recovery (TOPAZ) is based on a steady-state Look-Locker inversion-recovery, using segmented spoiled gradient-echo imaging of multiple cardiac phases. B_1^+ correction is performed in an integrated manner using the inversion-efficiency coefficient of a rectangular inversion pulse. Acquisition parameters are chosen to yield optimal T_1 mapping precision, based on numerical simulations. Accuracy and consistency of the T_1 time quantification across the cardiac phases are assessed using phantom imaging. In vivo imaging in healthy subjects is performed in a single breath-hold acquisition, and compared with a conventional myocardial T_1 mapping method.

METHODS

Sequence

The sequence diagram of the proposed TOPAZ acquisition is depicted in Figure 1. Initially, FLASH imaging pulses are used to drive the magnetization to steady state. An inversion pulse is then played, following the detection of the subsequent R-wave of the ECG signal. After the inversion, contiguous imaging throughout multiple heart beats is performed using FLASH pulses in a segmented fashion, until steady state is reached again. In this way, a k-space segment is acquired at each cardiac phase for several sample times on the inversion-recovery curve, where the inversion times for a given cardiac phase are separated by the duration of the R-R interval. After multiple heart beats, the magnetization is driven to steady state, and the acquisition of the next k-space segments begins with another inversion pulse played at the next R-wave. To avoid deviation from the pulsed steady-state recovery curve in the presence of R-R interval variations, dummy pulses, with no corresponding signal readout, are played after the acquisition of a predetermined number of cardiac phases until the detection of the subsequent R-wave.

Flip angle and repetition time (TR) were chosen based on numerical simulations to optimize TOPAZ T_1 mapping sensitivity. The number of segments was selected between 8 and 12, depending on the heart rate, to yield a scan time between 17 and 23 s.

Joint Reconstruction of Temporally Resolved T_1 and B_1^+ Maps

The magnetization signal during contiguous FLASH pulses can be described by a three-parameter inversion-recovery model (26) as follows:

$$M_z(t) = M_{SS} - \Big(M_{SS} - M_z(0)\Big) * \exp(-t/T_1^*), \quad [1]$$

where T_1^* describes an apparent T_1, which is a function of the FA and TR:

$$T_1^* = \left(\frac{1}{T_1} - \frac{1}{TR}\log\Big(\cos(\alpha)\Big)\right)^{-1}. \quad [2]$$

The magnetization inversion is performed from the steady-state signal using a rectangular hard pulse. Hence, for an inversion FA of α^{inv}, the initial signal can be described as

$$M_z(0) = M_{ss}\cos(\alpha^{inv}) \quad [3]$$

leading to the magnetization

$$M_z(t) = M_{ss}\Big(1 - \Big(1 - \cos(\alpha^{inv})\Big) * \exp(-t/T_1^*)\Big). \quad [4]$$

Thus, parameter quantification can be performed using a three-parameter least square fit as follows:

$$\begin{aligned}(\hat{A}, \hat{B}, \hat{T}_1^*)_j = &\arg\min_{A,B,T_1^*} \sum_k ||S\Big(t_k^{(j)}\Big) \\ &- \Big(A\Big(1 - B * \exp\Big(-t_k^{(j)}/T_1^*\Big)\Big)\Big)||^2,\end{aligned} \quad [5]$$

for $j = 1, \ldots, C$, in which C is the number of cardiac phases, $t_k^{(j)}$ denotes the inversion time of the kth T_1-weighted image of the jth cardiac phase, and $S\Big(t_k^{(j)}\Big)$ is the corresponding signal for a given pixel location.

As the B parameter describes the inversion efficiency, phase-resolved B_1^+ information can be estimated from the three-parameter fit. When a nominal inversion FA of α_{nom}^{inv} is used, $\beta = \cos^{-1}(B-1)/\alpha_{nom}^{inv}$ results in the temporally resolved pixel-wise B_1^+ FA scaling factor and can be used as a B_1^+ map. Accordingly, the actual excitation FA can be derived from the three fit parameters as

$$\frac{\alpha^{exc}}{\alpha_{nom}^{exc}} \approx \frac{\alpha^{inv}}{\alpha_{nom}^{inv}} = \beta = \frac{\cos^{-1}(B-1)}{\alpha_{nom}^{inv}}. \quad [6]$$

Here, α^{exc} describes the nominal excitation FA after compensation for slice-profile effects. Details of the slice-profile correction are provided in the Appendix and Supporting Figures S1 to S3. The T_1 time can then be derived from the three fit parameters as

$$\begin{aligned}T_1 &= \left(\frac{1}{\hat{T}_1^*} - \frac{1}{TR}\log\Big(\cos(\alpha^{exc})\Big)\right)^{-1} \\ &\approx \left(\frac{1}{\hat{T}_1^*} - \frac{1}{TR}\log\left(\cos\left(\alpha_{nom}^{exc}\frac{\cos^{-1}(\hat{B}-1)}{\alpha_{nom}^{inv}}\right)\right)\right)^{-1}.\end{aligned} \quad [7]$$

In this study, the three-parameter fitting in Equation [5] was performed using a bounded parameter range for the inversion efficiency ([1.4 2.4]), to avoid detrimental effects of outliers in the B_1^+ maps of late heart phases.

Numerical Simulations

The sensitivity of the parameter estimation is a function of the T_1, the FA, and the TR in TOPAZ T_1 mapping. Numerical Monte-Carlo simulations were performed to optimize the T_1 time precision in dependence on the sequence parameters. The signal throughout the proposed sequence was simulated using Bloch simulations. Rician noise characteristics were achieved by adding complex noise with independently normal distributed real and imaginary part and using the absolute value for further analysis. Simulations were performed with a heart rate of 60 bpm, no B_1^+ variations, and a tissue T_1 time of 1550 ms to resemble healthy myocardial tissue at 3 T (19). Noise was simulated at a signal-to-noise ratio of 30 relative to the steady-state magnetization for parameters TR = 4.5 and FA = 4.4° (Ernst angle). T_1 time accuracy was obtained as the difference between the mean of the estimated T_1 across 1000 noise patterns and the simulated ground-truth T_1 time. T_1 time precision was calculated as the standard deviation across the noise patterns.

To ensure sufficient recovery before the reinversion, the number of heart beats between the inversion pulses in the simulated sequence was adapted to allow for recovery to at least 95% of the steady-state signal, for each (TR, FA) pair and the given T_1 value. This leads to different scan times for different (TR, FA) settings and restricts the applicable parameter range, to avoid long breath-hold durations. The simulated parameter range spanned from 1° to 20° degrees FA in steps of 1°, and 3.5 to 15.0 ms TR in steps of 0.5 ms.

Phantom Experiments

All imaging was performed at a 3 T Siemens Magnetom Prisma (Siemens Healthcare, Erlangen, Germany) system using a 30-channel receiver coil-array.

The proposed method was compared with inversion-recovery spin-echo T_1 mapping (16) in a cylindrical phantom containing several compartments filled with gadolinium-doped agarose gel to achieve T_1 and T_2 times in the in vivo range (T_1/T_2 = 390/70, 696/84, 1233/106, 1665/442, 2147/∼2000 ms (27)). Imaging was performed with a simulated ECG signal at 60 bpm. All T_1 maps were acquired with 10 repetitions. The TOPAZ T_1 times were assessed for all cardiac phases. Accuracy was defined based on manually drawn ROIs in comparison with saturation pulse prepared heart rate–independent inversion-recovery (SAPPHIRE) T_1 times. Spatial variability was assessed as a surrogate for precision by calculating the standard deviation of the T_1 time within the ROI drawn in the homogenous phantom compartment. Consistency in the T_1 time accuracy and precision are assessed as the coefficient of variation (COV).

The dependence of TOPAZ T_1 mapping on the heart rate was studied by acquiring images in the same phantom with various simulated ECGs. The R-R intervals were varied between 600 ms (100 bpm) and 1200 ms (50 bpm). For each manually drawn ROI, the T_1 time and spatial variation within the ROI were averaged across all phases. Dependence on the R-R interval of the simulated ECG was assessed using COV and correlation analysis.

Imaging sequence parameters for TOPAZ T_1 mapping were as follows, in the present study: TR/echo time (TE)/FA = 5/2.5 ms/3°, bandwidth = 350 Hz/Px, field of

view (FOV) = 300 × 225 mm^2, resolution = 1.9 × 1.9 mm^2, matrix size = 160 × 120, slice thickness = 10 mm, partial Fourier = 6/8, generalized autocalibrating partial parallel acquisition factor = 2, reference lines = 24 (in plane), number of phase-encode lines = 55, time between inversion pules = 5 to 6 R-R intervals, inversion pulse: 0.5 ms rectangular pulse (160° FA, to ensure the acos is well defined, which allows for estimation of the B_1^+ amplitude using Eq. [6]), excitation pulse: symmetrical sinc pulse with bandwidth-time product = 2.0, temporal resolution = 40 to 60 ms, breath-hold duration = 17 to 23 s.

Reference T_1 times were acquired using an inversion-recovery spin-echo sequence, with TR/TE/FA = 10 s/12 ms/90°, bandwidth = 300 Hz/Px, FOV = 240 × 240 mm^2, resolution = 1.9 × 1.9 mm^2, slice thickness = 10 mm, inversion times = 50, 100, 200, ..., 6400 ms and one image without inversion pulse, scan time = 3 h 12 min.

In Vivo Experiments

The imaging protocol was approved by the local institutional review board, and written informed consent was obtained from all participants before each examination for this HIPAA-compliant study. Cardiac phase-resolved T_1 maps were obtained from nine healthy subjects (4 male, 32 ± 15 years old) using the proposed TOPAZ T_1 sequence and compared with SAPPHIRE T_1 mapping (14). The TOPAZ sequence was acquired with the same imaging parameters as described for the phantom experiment. SAPPHIRE T_1 mapping was acquired for reference with FLASH imaging readout and the following parameters: TR/TE/FA = 4.0/2.0 ms/10°, bandwidth = 505 Hz/Px, FOV = 320 × 320 mm^2, resolution = 2.0 × 2.1 mm^2, matrix size = 160 × 152, slice thickness = 10 mm, slice gap = 10 mm, partial Fourier = 6/8, generalized autocalibrating partial parallel acquisition factor = 2, reference lines = 40 (in plane), number of phase-encode lines = 77, linear k-space ordering, number of images = 15, inversion pulse: 2.56 ms tan/tanh adiabatic full passage (28), and saturation pulse: four-compartment water suppression enhanced through T_1 effects (WET) pule (19).

All images were acquired in a single midventricular slice. Myocardial T_1 times were assessed throughout the entire cardiac cycle using manually drawn ROIs in the septal wall. In vivo precision was defined as the standard deviation within the septal ROI. Due to a different number of cardiac phases acquired with TOPAZ in volunteers with different heart rates, the vectors of septal T_1 times acquired with TOPAZ throughout the cardiac cycle had different lengths for each volunteer. To facilitate quantitative comparison among subjects, each vector of septal T_1 times was interpolated to 20 elements. T_1 times and T_1 precision between the methods were statistically compared using paired student's t-test and Wilcoxon signed-rank tests, respectively. T_1 times at different cardiac phases were compared for statistical significant differences using one-way analysis of variance. Differences in the precision across the cardiac phases were studied using Kruskal-Wallis group analysis. All statistical tests were compared at a significance level of $P < 0.05$.

Analysis of the estimated B_1^+ variation across cardiac regions and cardiac phases was performed by manually drawing profiles across the heart from the apex through the midseptum to the lateral wall in the B_1^+ maps, in all cardiac phases. To allow for intersubject comparison, B_1^+ values were interpolated to 20 virtual cardiac phases as described for T_1 time above and mean and standard deviation across all subjects were calculated as a function of cardiac region and cardiac phase. B_1^+ maps were quantitatively analyzed with respect to the B_1^+ gradient along the line from the apex through the midseptum to the lateral free wall. Linear trends were compared among the cardiac phases using Pearson's correlation coefficient, and statistically compared using analysis of variance following Fisher's Z-transformation. Furthermore, the slope of the spatial gradient was calculated and statistically compared among subjects.

RESULTS

Numerical Simulations

Figure 2 depicts the precision, accuracy, and duration of the proposed technique as functions of TR and FA. High FAs and short TRs cause rapid recovery to the steady-state magnetization. This prevents accurate T_1 estimation and hampers the estimation precision. In contrast, low FAs, well below the Ernst angle, result in compromised T_1 mapping precision as a result of insufficient imaging signal-to-noise ratio. Long TRs increase the duration of the recovery and the steady state signal, leading to improved precision, although at the cost of prolonged scan time. A TR of 5 ms and FA of 3° were chosen as a trade-off between T_1 mapping precision and scan time, in the remainder of the study. This setting requires five R-R intervals of pulsed recovery before re-inversion of the magnetization at a heart rate of 60 bpm.

Phantom Experiments

Figure 3 shows the results of the T_1 time measurement in phantom. The effect of the proposed B_1^+ correction is depicted in Figure 3a, where severe underestimation of the T_1 time compared with spin-echo measurements is observed without any correction for excitation FAs ($y = 0.77\,x + 91$ ms). Corrected T_1 times are in good agreement with spin-echo measurements, showing only slight deviations (−1.1 to 7.5%, $y = 1.04\,x - 29$ ms, normalized root mean square error = 4.2%). Figure 3b shows the estimated T_1 times and the precision as a function of the cardiac phase. The TOPAZ T_1 times show high consistency throughout the cardiac cycle (COV = 1.4 ± 0.78%), although slight reduction in precision is observed in the later cardiac phases.

The evaluation of TOPAZ T_1 times at different heart rates is shown in Figure 4. Good consistency of the average T_1 across a wide range of R-R intervals is observed, resulting in a COV of 1.2 ± 1.9%. No correlation with the R-R interval is observed across the phantom T_1 times (R = 0.0026). A slight trend of increased spatial variability is observed at longer R-R intervals (COV = 34.4 ± 23.3%, R = 0.54), in which more cardiac phases are sampled at the expense of fewer time points on the inversion-recovery curve. This trend is particularly pronounced for the shortest T_1 time (COV = 73.6%,

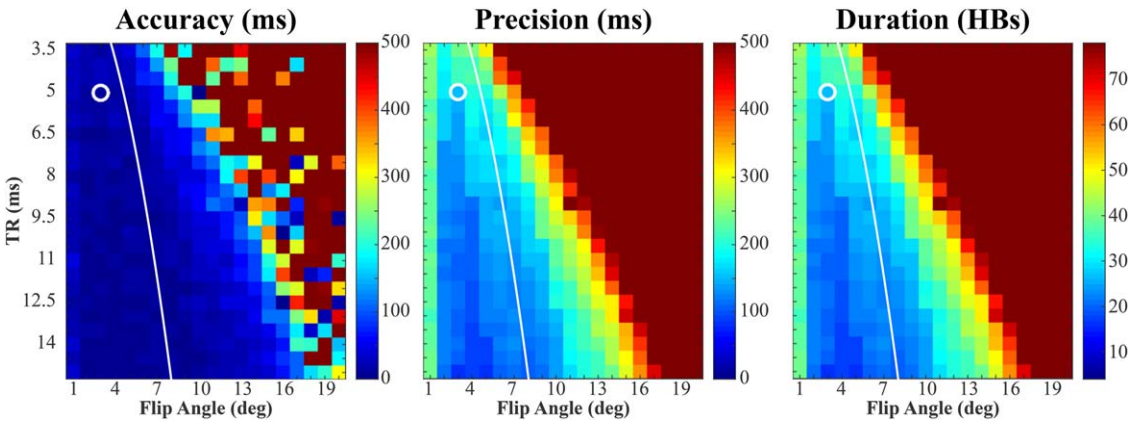

FIG. 2. Simulation results depicting phantom accuracy, precision, and sequence duration as a function of TR and FA, as assessed using noisy Bloch simulations. The white line indicates the Ernst angle for each TR/FA pair, yielding optimal signal strength in a conventional, continuous FLASH acquisition. High FAs and short TRs impair sensitivity to the T_1 time and substantially compromise fit accuracy and precision. Long TRs and low FAs, in contrast, result in long recovery periods, leading to increased scan time. Based on the simulation results, a TR of 5 ms, and FA of 3° (white circle) were selected as a compromise, resulting in 1559 ± 151 ms (T_1 time ± precision, simulated T_1: 1550 ms) and scan duration of 25 heart beats.

R = 0.95), which leads to the fastest recovery to the pulsed steady state, and requires a denser sampling of the beginning of the inversion-recovery curve.

In Vivo Experiments

Representative baseline images of an exemplary TOPAZ scan with 50-ms temporal resolution are shown in Figure 5 along with the corresponding T_1 maps (all six inversion times and twelve cardiac phases for this subject are shown in Supporting Fig. S4). Raw images show strong inversion-recovery contrast, with differential signal changes of the myocardium and the blood pool signal intensity. Zero-crossing of the myocardial signal happens around one R-R interval after the inversion pulse.

Figure 6 shows example TOPAZ T_1 and B_1^+ maps of selected cardiac phases acquired in a healthy subject at a temporal resolution of 40 ms (all cardiac phases are shown in Supporting Fig. S5). The T_1 maps show homogenous T_1 quantification throughout the myocardium at all cardiac phases. Sharp delineation toward the blood pools suggests sufficient temporal resolution to minimize temporal blurring of the myocardial contours. B_1^+ maps appear noise resilient and largely T_1 insensitive at the earlier phases. However, increased inhomogeneity and compromised B_1^+ precision is observed at the later cardiac phases. Additional examples of phase-resolved T_1 maps are provided as quantitative movies in Supporting Videos SV1 to SV3.

Figure 7 depicts diastolic and systolic phases of the TOPAZ T_1 maps, as well as the comparison SAPPHIRE T_1 maps acquired as a single temporal snapshot during diastole. As with phantom imaging, uncorrected TOPAZ T_1 maps show severe underestimation compared with SAPPHIRE T_1 maps. This is mitigated using the

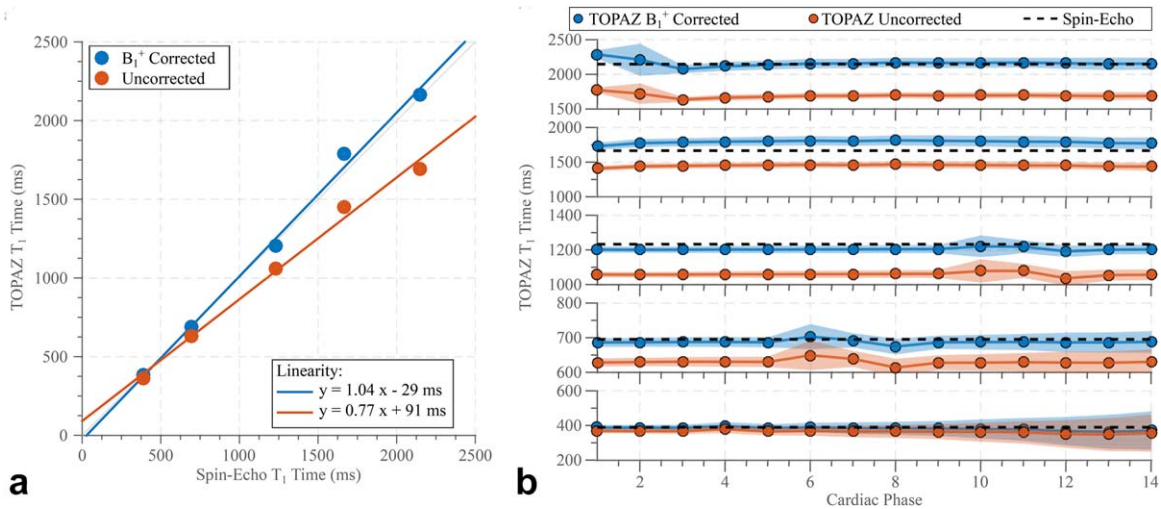

FIG. 3. **a**: Phantom TOPAZ T_1 values averaged across phases compared with spin-echo T_1 values show substantial underestimation without B_1^+ correction. Good agreement is obtained with the corrected method. **b**: Phantom accuracy and precision of the proposed TOPAZ T_1 mapping method (represented by circles and intervals, respectively) are compared across all cardiac phases. The estimated T_1 times are consistent and accurate across cardiac phases and T_1 values, although slight deviation in precision is observed in later cardiac phases for lower T_1 values.

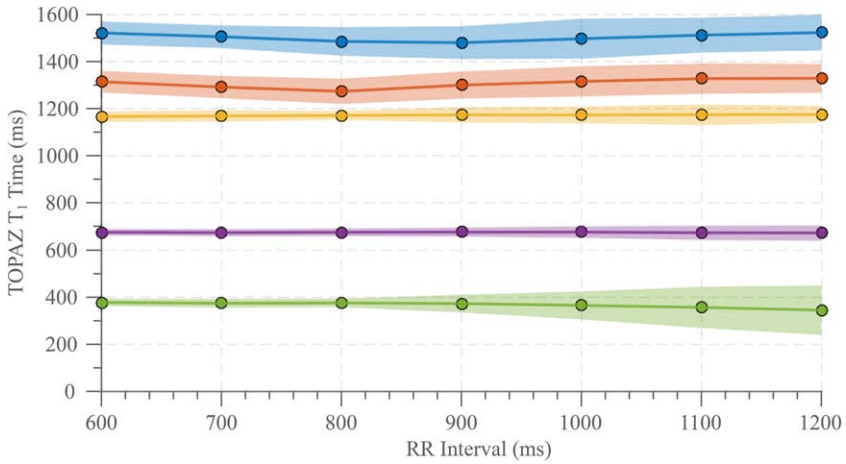

FIG. 4. T_1 time and spatial variability, averaged across all cardiac phases, are acquired with TOPAZ T_1 mapping at different simulated R-R intervals. Good consistency of the T_1 time is obtained across a wide range of simulated heart rates. A slight trend of increased spatial variability is observed at long R-R intervals, especially for very short T_1 times, as a result of insufficient sampling of the early part of the inversion-recovery curve.

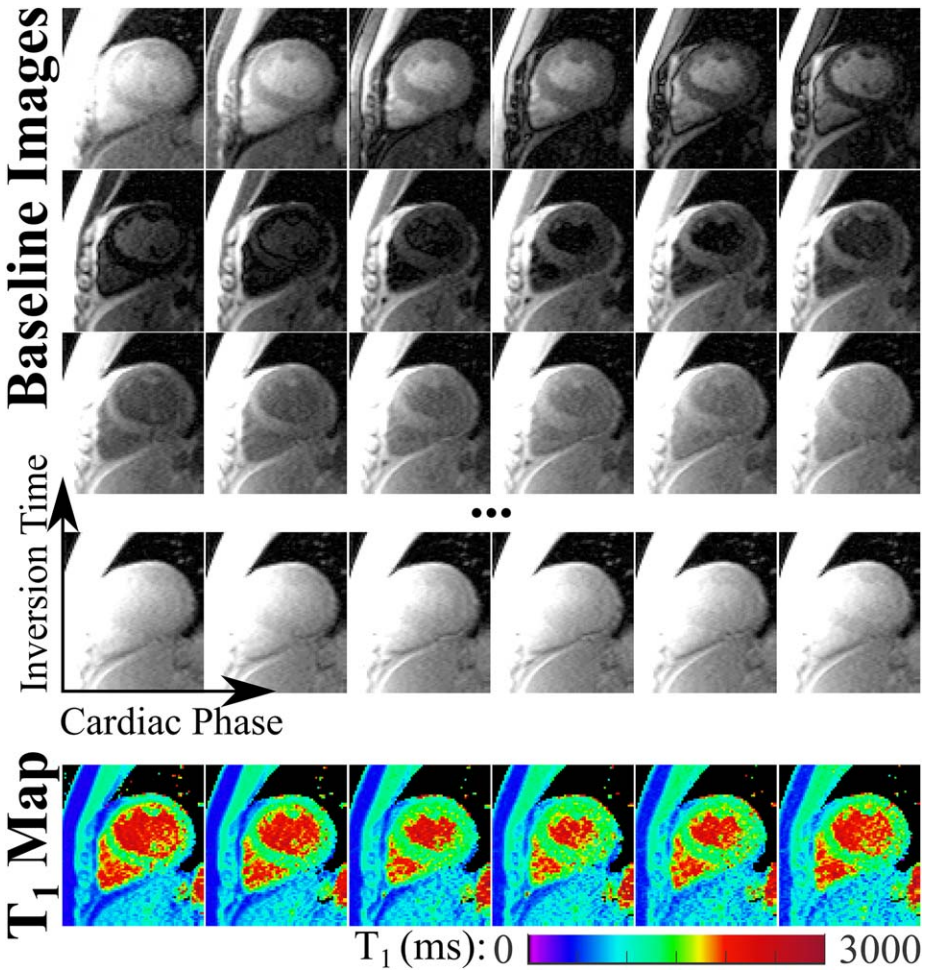

FIG. 5. Representative baseline images show four inversion times at six cardiac phases acquired in a healthy subject with the proposed TOPAZ T_1 mapping sequence. All images are displayed with the same window level. Visually high contrast is depicted between the myocardium and the blood pools in the earlier images before the zero crossing, which happens around the time of one R-R interval after the inversion pulse. Longer inversion times depict higher overall signal and weaker contrast, displaying increased proton density weighting. The corresponding T_1 maps show comparable T_1 times across the cardiac cycle. Visually decreased homogeneity is observed in the later phases, which is in accordance with the decreased dynamic signal range. All six inversion times at 12 cardiac phases with 50 ms temporal resolution are provided in Supporting Figure S4.

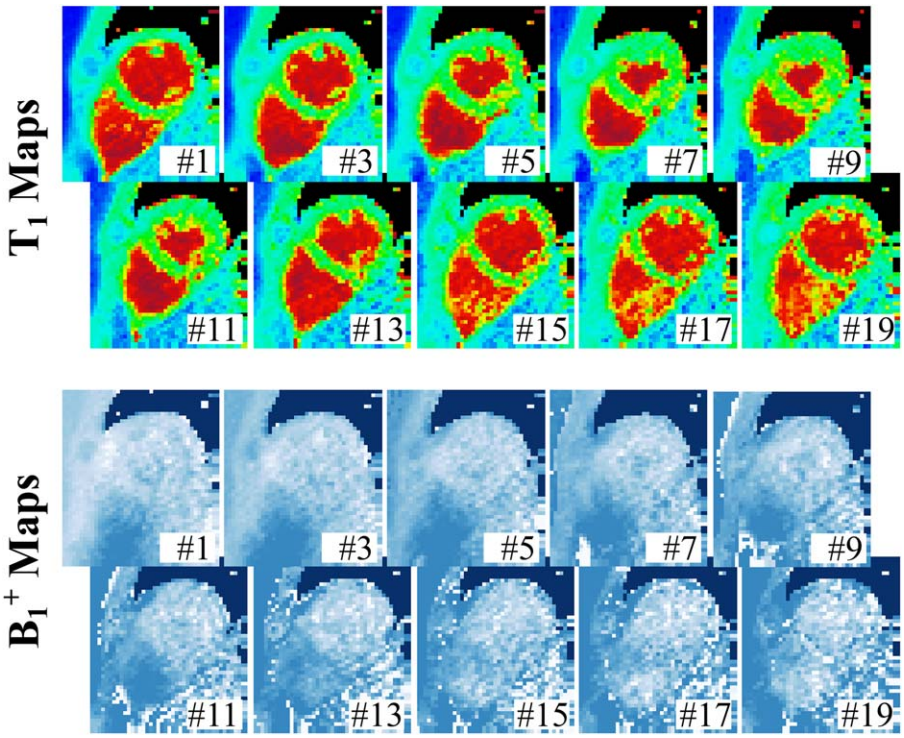

FIG. 6. In vivo T_1 and B_1^+ maps jointly acquired in a healthy subject with TOPAZ T_1 mapping, at representative cardiac phases acquired with a temporal resolution of 40 ms. Visually high T_1 map quality with homogeneous signal in the myocardium is observed. Good B_1^+ quality is observed at the earlier heart-phases, but is degraded toward the end of the cardiac cycle. T_1 and B_1^+ maps of all cardiac phases for this subject are provided in Supporting Figure S5.

proposed joint estimation of B_1^+ maps for correction of the apparent T_1 time, yielding T_1 maps that are comparable to SAPPHIRE maps in terms of visual quality.

Average myocardial T_1 times and T_1 time precision were quantified throughout the cardiac cycle across all subjects, as shown in Figure 8, along with T_1 maps of a

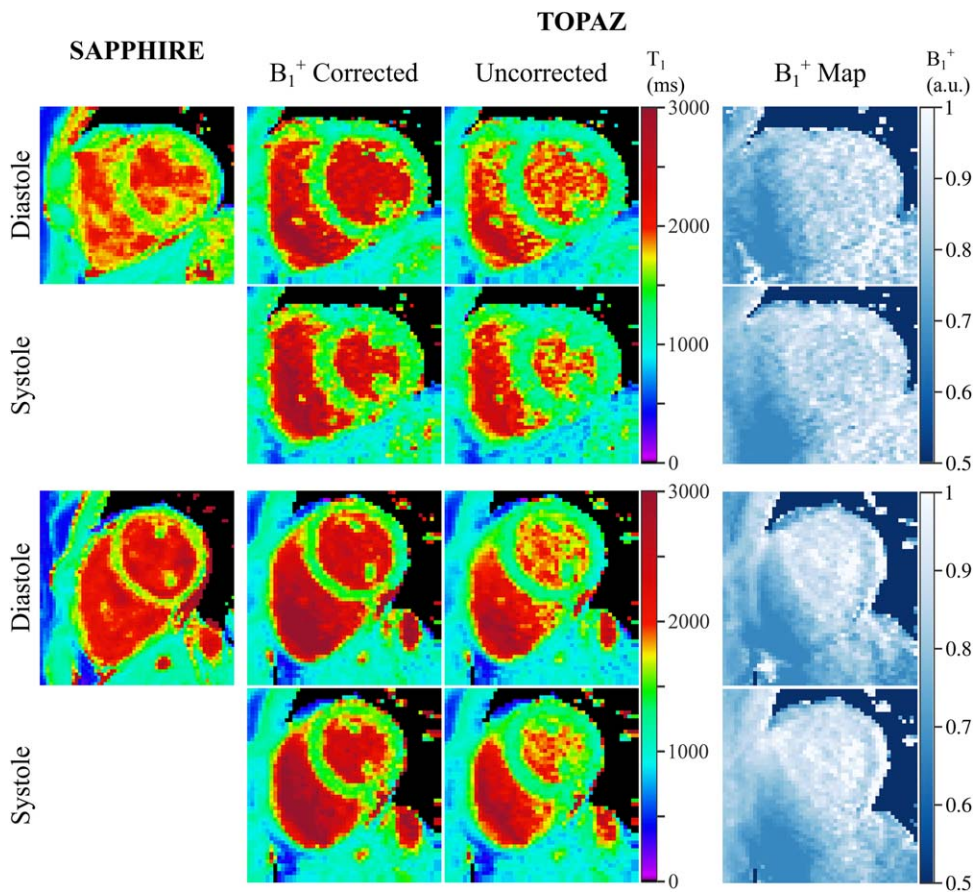

FIG. 7. Representative diastolic T_1 maps acquired with SAPPHIRE compared with a systolic and diastolic phase acquired with the proposed TOPAZ T_1 mapping method. The TOPAZ T_1 maps are shown before and after B_1^+ correction along with the B_1^+ maps used in the correction. As in phantom imaging, the corrected TOPAZ T_1 maps are consistent with conventional SAPPHIRE T_1 maps. The B_1^+ maps obtained from the joint estimation do not show substantial spatial variation for these cardiac phases.

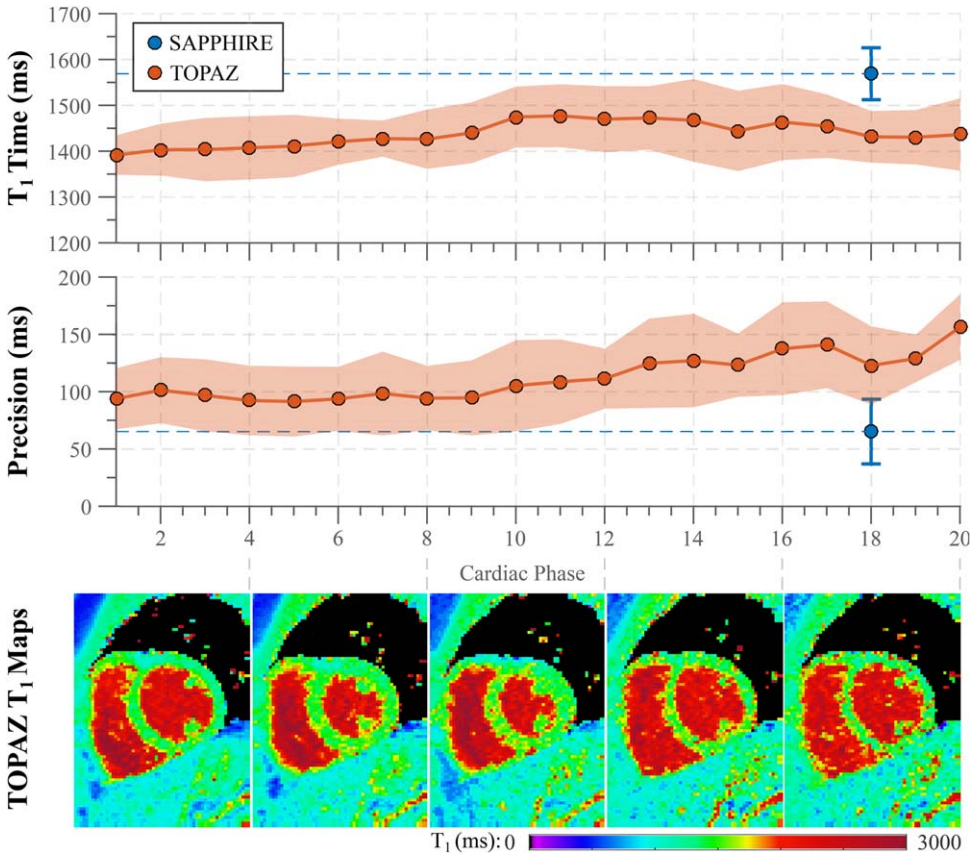

FIG. 8. Myocardial T_1 times and in vivo precision of TOPAZ T_1 mapping are shown at 20 interpolated cardiac phases. The top row displays the mean T_1 time per subject, averaged over all healthy volunteers. The middle row depicts the standard deviation within the septal ROI of a subject averaged across the cohort. Shadings indicate the standard deviation across the nine subjects. In the bottom row, five myocardial T_1 maps that are representative of the trend throughout the cardiac cycle are presented. Consistent T_1 times with no major variation are achieved across the cardiac cycle. Early phases show good in vivo precision, comparable to SAPPHIRE T_1 mapping. A trend of increased in vivo variability is observed in the later phases of the cardiac cycle.

single subject at five representative cardiac phases. Additionally, the average and standard deviation of in vivo B_1^+ corrected and uncorrected T_1 times, as well as precision and B_1^+ amplitude, are listed for all cardiac phases in Table 1. At peak systole and peak diastole, the T_1 times acquired using the TOPAZ sequence were 1475 ± 66 ms and 1431 ± 56 ms. This indicates a 5.9% and 8.6% decrease compared with SAPPHIRE T_1 mapping (1569 ± 65 ms, $P < 0.01$). Slightly elevated T_1 time was found during end systole, but with no significance in the difference between the cardiac phases (analysis of variance: $P = 0.14$, $\mathrm{COV} = 3.2 \pm 0.8\%$). In vivo precision was comparable to SAPPHIRE T_1 mapping at early heart phases ($P > 0.07$), but showed a significant increase toward the end of the cardiac cycle (Kruskal-Wallis: $P < 10^{-3}$, compared with SAPPHIRE: $P < 0.004$).

Figure 9 depicts the results of the B_1^+ variation analysis as a function of cardiac regions and cardiac phases. The profiles exhibit dependence on cardiac regions, with a trend of increased B_1^+ amplitude from the apex to the lateral wall. They also show an increase in B_1^+ inhomogeneity in later cardiac phases, in accordance with the unfavorable conditioning for the joint estimation in these cardiac phases. The correlation coefficient between B_1^+ amplitude and the spatial location as well as the spatial gradient slope of the B_1^+ amplitude are fairly consistent over the earlier phases, but detriment toward the end of the cardiac cycle (analysis of variance for correlation coefficient: $P < 10^{-9}$, slope $< 10^{-4}$).

DISCUSSION

In this study, we developed a sequence to acquire cardiac phase-resolved native T_1 maps of the myocardium, with integrated B_1^+ quantification at a temporal resolution of up to 40 ms in a single breath-hold. The sequence parameters for the proposed TOPAZ T_1 mapping sequence were optimized numerically. High accuracy and good consistency of the T_1 times across the cardiac phases and at different heart rates were achieved in phantom measurements, while in vivo maps showed slight underestimation of the myocardial T_1 times.

Native myocardial T_1 mapping is an emerging tool, establishing itself in the cardiovascular MRI sequence portfolio for diagnosis, risk stratification, and prognosis of numerous cardiomyopathies. However, large-scale clinical evaluation has commenced only recently, and limited exposure of clinicians to this technique likely hampers its diagnostic value. Signal originating from different structures, such as the myocardial muscle, the blood pools or extra cardiac fat, exhibit severely distinct T_1

Table 1
Cardiac Phase-Resolved Quantification of T_1 Across Nine Healthy Subjects.

Cardiac Phase	1	2	3	4	5	6	7	8	9	10
T_1 time (ms)	1391.6 ± 43.2	1403.3 ± 56.4	1403.6 ± 68.9	1407.3 ± 68.9	1411.4 ± 67.8	1420.7 ± 50.2	1427.4 ± 39.5	1426.2 ± 64.6	1440.1 ± 66.3	1474.6 ± 66.4
Precision (ms)	94.0 ± 26.7	101.4 ± 28.8	96.9 ± 31.5	92.4 ± 30.3	91.5 ± 30.6	93.8 ± 28.0	98.5 ± 36.5	94.5 ± 28.2	94.7 ± 32.7	105.3 ± 39.8
T_1^* time (ms)	1212.0 ± 39.5	1225.6 ± 47.4	1227.1 ± 56.8	1231.2 ± 60.8	1236.0 ± 59.0	1244.6 ± 40.8	1249.3 ± 31.2	1246.4 ± 51.8	1256.6 ± 51.3	1287.3 ± 53.7
Relative B_1^+ (%)	87.4 ± 5.6	86.0 ± 4.2	85.6 ± 3.8	85.3 ± 4.3	84.9 ± 4.1	84.4 ± 3.1	84.6 ± 3.2	85.2 ± 3.2	85.3 ± 2.9	84.2 ± 2.9
Cardiac Phase	11	12	13	14	15	16	17	18	19	20
T_1 time (ms)	1477.2 ± 68.5	1469.8 ± 71.9	1472.5 ± 69.1	1467.2 ± 90.2	1444.3 ± 87.4	1463.5 ± 82.9	1454.4 ± 69.1	1431.3 ± 56.2	1430.4 ± 59.3	1436.3 ± 78.8
Precision (ms)	108.8 ± 36.9	111.4 ± 26.2	124.9 ± 39.0	127.2 ± 40.8	123.2 ± 27.6	137.6 ± 40.5	141.0 ± 37.9	122.9 ± 34.2	129.0 ± 20.7	156.5 ± 28.6
T_1^* time (ms)	1289.6 ± 56.2	1282.9 ± 58.2	1284.4 ± 58.5	1281.3 ± 79.6	1262.0 ± 74.0	1280.5 ± 70.2	1273.9 ± 59.5	1250.4 ± 53.7	1247.7 ± 56.2	1251.9 ± 73.6
Relative B_1^+ (%)	84.2 ± 2.9	84.5 ± 2.7	84.8 ± 3.1	84.5 ± 3.8	85.0 ± 3.5	84.1 ± 3.4	84.1 ± 3.4	85.7 ± 4.1	86.5 ± 4.5	86.7 ± 6.3

Note: T_1 time depicts the B_1^+ corrected T_1 time assessed in manually drawn ROIs in the septum of the myocardium. Precision shows the spatial variation within the ROI. T_1^* time provides the relaxation time without B_1^+ correction. Relative B_1^+ gives the measured B_1^+ amplitude relative to the nominal B_1^+ amplitude. All data sets were up-sampled to 20 cardiac phases for quantitative analysis. All reported values are the mean and standard deviations per up-sampled cardiac phase across healthy subjects.

characteristics and need to be carefully delineated to maximize the diagnostic quality of T_1 mapping. T_1 mapping during systole was proposed to increase the readily evaluable myocardial area and to facilitate manual contouring. Recently, blood-suppressed myocardial T_1 mapping was also introduced to eliminate contamination of the myocardial signal by the neighboring blood pool (29). Both approaches yield increased resilience to ROI placement and decreased observer variability. The proposed TOPAZ technique might further increase the diagnostic confidence in myocardial T_1 maps by presenting quantification at multiple phases throughout the heartbeat. This might ease the delineation of blood, subepicardial fat and other structures, and altered T_1 times observed in a single phase can be substantiated by cross-comparison throughout the cardiac cycle. Thus, the technique might be particularly useful in diseases, which form complicated focal/diffuse scar patterns such as hypertrophic cardiomyopathy or amyloidosis. A recent study has demonstrated that in healthy volunteers, who usually have thin myocardial walls, quantitative tissue characterization is sensitive to slice orientation, myocardium thickness, and wall motion (30)—a problem that cannot be easily alleviated by improved ROI placement. T_1 mapping throughout the myocardial cycle, at various states of myocardial contraction, could improve robustness in this cohort, and therefore minimize false positive outliers. Accordingly, patients exhibiting pathologically decreased myocardial wall thickness, such as when suffering from dilated cardiomyopathy, might benefit from the proposed technique.

Conventional myocardial T_1 mapping methods use single-shot imaging over a window of 150 to 250 ms to allow the acquisition of a single T_1-weighted snapshot of the heart per heartbeat. This temporal resolution is sufficient for imaging the left-ventricular myocardium during the end-diastolic quiescence in most patients and healthy volunteers. However, the achieved temporal resolution is often insufficient to quantify highly mobile extra myocardial structures, such as cardiac tumors, including myxomas, or thrombi. Also, the long acquisition windows of single-shot sequences have been shown to impair quantitative cardiac mapping, even in healthy volunteers, when residual motion is abundant in middiastole (30). Finally, patients suffering from wall motion abnormalities, including bundle branch blocks, commonly exhibit low image quality in diastolic imaging. The proposed method enables imaging at a temporal resolution of up to 40 ms. Conventional cine imaging at this temporal resolution has been proven valuable in depicting even highly mobile structures (31). Hence, the proposed method might be used for improved characterization of subjects with residual diastolic motion or motion abnormalities. Furthermore, it might extend the applicability of T_1 quantification to extra-myocardial structures, potentially easing noninvasive characterization or classification of cardiac masses, such as myxomas or other tumors. Further evaluation of the proposed technique in this patient cohort is warranted to assess diagnostic sensitivity.

High accuracy and minimal deviation from the reference method were shown for the proposed technique in phantom scans, over a wide range of T_1 times. However, in vivo quantification of the myocardial T_1 times show underestimation

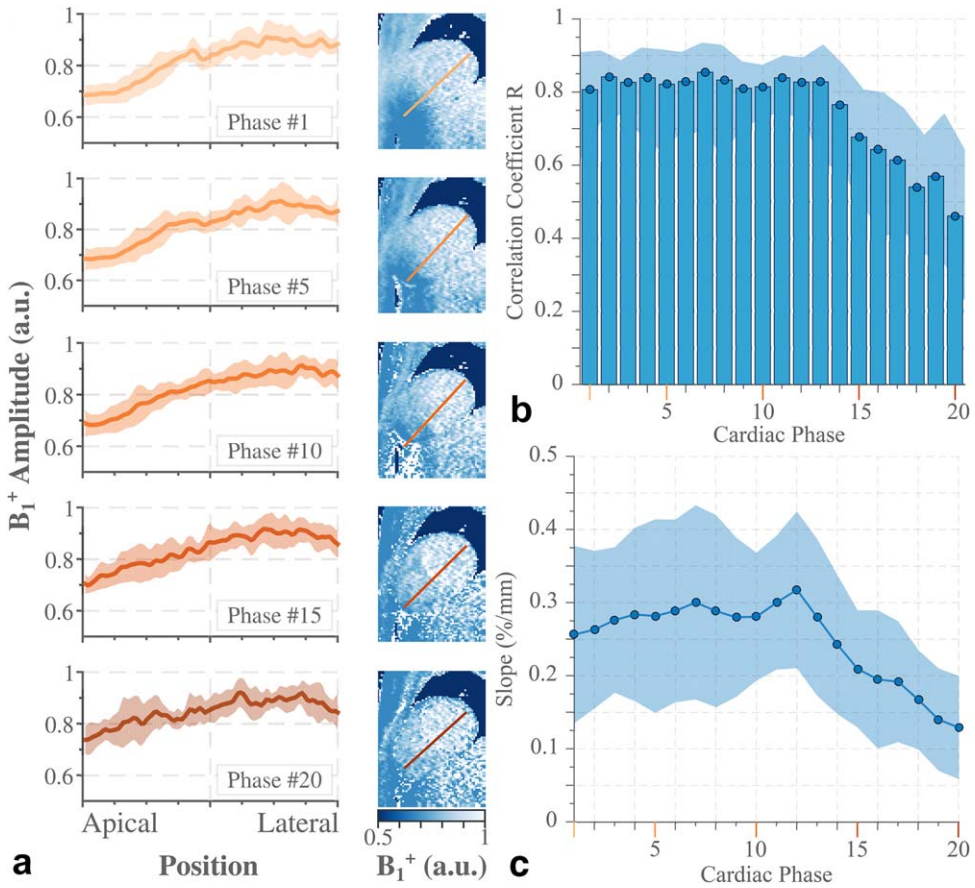

FIG. 9. Quantitative analysis of the B_1^+ profiles obtained with the proposed TOPAZ sequence. **a**: The left panel depicts B_1^+ trends across the heart at five representative cardiac phases, as the mean and standard deviation across all healthy subjects. The right panel shows B_1^+ maps of a single healthy subject, including the spatial location of the B_1^+ profile. A trend of increased B_1^+ amplitude from apex to the lateral free wall is consistently observed across all cardiac phases and across all subjects. B_1^+ maps at later phases have a tendency of increased variability, especially in apical locations. **b**: Correlation statistics of the B_1^+ amplitude to the spatial location. A strong linear trend indicated by high correlations is shown consistently in the earlier phases, with the trend mitigating toward the end of the cardiac cycle. **c**: Slope of spatial B_1^+ gradient from apex to lateral wall as average and standard deviation over all subjects. A comparable slope is maintained over the beginning of the cardiac cycle. A decreased B_1^+ gradient is observed in the later phases.

of approximately 10% compared with SAPPHIRE T_1 times, which are well in line with previous studies (19,32). Because of the use of a B_1^+ adjusted correction of the apparent T_1^* time in the present method, this level of accuracy still compares favorably to previously reported accuracy obtained with commonly used inversion-recovery–based myocardial T_1 mapping methods at 3 T and saturation-recovery methods as reference (19,20).

Accurate T_1 quantification in the proposed sequence requires imaging of the magnetization during the approach to the pulsed steady state. Cardiac motion will cause displacement of the heart within the inhomogeneous B_1^+ field. This induces cyclic changes in the effective FA and the apparent relaxation time. The accuracy of an estimation using a constant relaxation time might therefore be impaired in vivo. However, our data and previous cardiac B_1^+ papers (33,34) indicate the slope of the B_1^+ amplitude gradient being low. Given the current sequence parameters, this leads to less than 0.1° FA variation throughout the cardiac cycle, which can be expected to impair the estimation only marginally. More importantly, as a result of nonrigid cardiac motion, myocardial tissue that is not subjected to the previous excitation pulses, may move into the imaging plane and corrupt the signal. Although we have used a 10-mm slice thickness, a further increase in slice thickness, as well as a flat slice profile, reduce sensitivity at the edges of the slice excitation to through-plane motion and may be used at the cost of reduced spatial resolution. The effect of through-plane motion may be more pronounced in other views, such as two-chamber or horizontal long axis. Such effects were not explored in this introductory study, and warrants further investigation. Three-dimensional imaging might be used to ensure excitation of the entire cardiac volume, mitigating effects of through-plane motion. However, the corresponding increase in acquisition time requires other means of respiratory motion compensation, such as navigator gating and slice tracking, as previously proposed for myocardial T_1 mapping (13,35,36). Development of 3D free-breathing extensions of our technique requires further investigation.

In the proposed sequence, the transmit field strength was quantified based on the inversion efficiency of a rectangular inversion pulse. To ensure a unique solution to the inverse problem from the efficiency to the inversion FA, a FA smaller than 180° was chosen. However, T_1^* recovery, magnetization transfer effects, and B_0

inhomogeneities (off-resonances) compromise inversion efficiency and might corrupt the accuracy of the B_1^+ maps (37). Furthermore, B_1^+ sensitization is only performed at one time point throughout the cardiac cycle, at the time of inversion. Hence, flow and motion effects will affect the B_1^+ profiles at later cardiac phases. Nonetheless, the proposed B_1^+ mapping shows high visual quality and similar trends compared with B_1^+ maps obtained with dedicated methods in previous studies (33,34,38), with a consistent increase of B_1^+ amplitude from the apex to the lateral wall.

Sequential flipping (10) was used in this study for polarity restoration in the magnitude images. In phantom imaging, for the vial with $T_1 = 1233$ ms and at a single cardiac phase (700 ms after R-wave), this leads to points near the zero-crossing, eventually causing increased standard deviation in the T_1 measurements. Although this effect was not observed for myocardial T_1 values in the in vivo range, it can be further mitigated by the use of a phase-sensitive reconstruction (39).

Increased variability is observed toward the end of the heart beat in both B_1^+ and T_1 estimates. This is likely explained by the increased minimal inversion times at these phases, in which the earlier parts of the inversion-recovery curve were not sampled. This hampers the differentiation between T_1 and B_1^+ effects in the fit. To mitigate the effects of outliers in the B_1^+ map at later phases on the T_1 time precision, bounded fitting was performed by restricting the inversion efficiency to an expected range based on literature values (33). However, previously proposed methods for cardiac transmit field mapping did only allow for the generation of a single B_1^+ map. This prevents the application of quantitative methods throughout the entire cardiac cycle. The proposed method, in contrast, provides B_1^+ estimation at 40 ms temporal resolution in an integrated manner with T_1 mapping, at the cost of increased B_1^+ variability in parts of the cardiac cycle.

Tissue characterization following injection of contrast agents has proven clinical value in the form of late-gadolinium enhancement imaging (40) and quantification of extracellular volume quantification (41). For TOPAZ, the interrelation among quantification sensitivity, sequence parameters, and T_1 time might cause suboptimal performance in the postcontrast T_1 range with the presented scheme. Faster T_1 recovery requires fewer heart beats to reach steady state magnetization, and enables the acquisition of multiple inversion-recovery experiments during a single breath-hold. Furthermore, optimal precision is likely to be achieved at different FA and TR values, and separate optimization for the postcontrast T_1 regime is warranted. Phase-resolved extracellular volume mapping can be enabled by the acquisition of phase-resolved native and postcontrast T_1 maps. This additionally requires coregistration of the native and postcontrast maps, as previously proposed (42,43). High temporal resolution in the dynamic T_1 maps can be used to ensure adequate synchronization of the cardiac phases in the separate scans. Therefore, residual motion between matched cardiac phases in the two T_1 mapping acquisitions can be expected to be largely caused by variations in the end-expiratory breath-hold position.

Limitations

This study and the proposed method have several limitations. T_1 mapping was performed of the native myocardium only, and postcontrast application remains the subject of future studies. Slice thickness of 10 mm was used as a trade-off between through-plane motion sensitivity, signal-to-noise ratio, and spatial resolution. This slice thickness is used in several recent studies (44–48). However, reduced slice thickness is recommended for increased sharpness of the blood–myocardial interface (49).

The breath-hold duration of 17 to 23 s might not be accomplishable by some patients, although this is in line with some clinical cine protocols. Alternative parameter choices allow the trade-off between scan time and temporal and spatial resolution to be tailored to the actual target population in future studies. Furthermore, advanced undersampling and acceleration techniques, such as compressed sensing with temporal regularization, might be applied to drastically shorten the acquisition time and are currently being investigated (50). Furthermore, a rectangular FOV with a relatively low extent in the y-dimension was used in this study. For larger patients, an increase in FOV would cause either a coarser resolution or longer scan time. Although this was not an issue in the subject cohort for this study, such trade-offs may be necessary in clinical settings, and requires further exploration into higher acceleration approaches. Finally, no pathologies were evaluated in this proof-of-concept study, and evaluation of the diagnostic benefit over single-phase T_1 mapping is warranted in a separate study.

CONCLUSIONS

This study demonstrates the feasibility of cardiac phase-resolved T_1 mapping at a temporal resolution of 40 ms. The proposed TOPAZ T_1 mapping technique also allows for integrated acquisition of temporally resolved T_1 and B_1^+ maps. High-quality in vivo quantitative maps are obtained throughout the entire cardiac cycle. This bears promise to improve diagnostic confidence in myocardial T_1 mapping, by easing the delineation of surrounding structures.

APPENDIX

The signal at time t with FA α is given by

$$S(t,\alpha) = M_{SS}(\alpha) \cdot \underbrace{\left(1 - 2e^{-t\left(\frac{1}{T_1} - \frac{1}{TR}\log\left(\cos(\alpha)\right)\right)}\right)}_{:= R(t,\alpha)}, \quad [A1]$$

where

$$M_{SS}(\alpha) = \frac{\sin(\alpha)\left(1 - e^{-\frac{TR}{T_1}}\right)}{1 - \cos(\alpha)e^{-\frac{TR}{T_1}}}. \quad [A2]$$

For notational brevity we use $E(t,\alpha) = e^{-t\left(\frac{1}{T_1} - \frac{1}{TR}\log\left(\cos(\alpha)\right)\right)}$. We expand $R(t,\alpha)$ as a Taylor series with respect to α as follows:

$$\frac{\partial}{\partial\alpha}R(t,\alpha)=\frac{2t\cdot\tan(\alpha)\cdot E(t,\alpha)}{TR} \quad [A3]$$

$$\frac{\partial^2}{\partial\alpha^2}R(t,\alpha)=-\frac{2t\cdot E(t,\alpha)}{TR^2}\left(t\cdot\tan^2(\alpha)-TR\cdot\sec^2(\alpha)\right) \quad [A4]$$

$$\frac{\partial^3}{\partial\alpha^3}R(t,\alpha)=\frac{2t\cdot E(t,\alpha)}{TR^3}\left(t^2\tan^3(\alpha)-3t\cdot TR\cdot\tan(\alpha)\sec^2(\alpha)+2TR^2\cdot\tan(\alpha)\sec^2(\alpha)\right) \quad [A5]$$

for $\alpha=0$, this yields

$$R(t,0)=1-2e^{-\frac{t}{T_1}} \quad [A6]$$

$$\frac{\partial}{\partial\alpha}R(t,\alpha)\Big|_{\alpha=0}=0 \quad [A7]$$

$$\frac{\partial^2}{\partial\alpha^2}R(t,\alpha)\Big|_{\alpha=0}=\frac{2te^{-\frac{t}{T_1}}}{TR} \quad [A8]$$

$$\frac{\partial^3}{\partial\alpha^3}R(t,\alpha)\Big|_{\alpha=0}=0 \quad [A9]$$

leading to

$$R(t,\alpha)=R(t,0)+\alpha\frac{\partial R(t,\alpha)}{\partial\alpha}\Big|_{\alpha=0}+\frac{\alpha^2}{2}\frac{\partial^2R(t,\alpha)}{\partial\alpha^2}\Big|_{\alpha=0}+\frac{\alpha^3}{6}\frac{\partial^3R(t,\alpha)}{\partial\alpha^3}\Big|_{\alpha=0}+O(\alpha^4)=\left(1-2e^{-\frac{t}{T_1}}\right)+\frac{te^{-\frac{t}{T_1}}}{TR}\alpha^2+O(\alpha^4) \quad [A10]$$

This approximation is illustrated in Supporting Figure 1.

The signal along a nonconstant slice profile $\alpha(x)$ is obtained as

$$S_{Slc}(t)=\int_x S\Big(t,\alpha(x)\Big)dx=\int_x M_{SS}\Big(\alpha(x)\Big)R\Big(t,\alpha(x)\Big)dx. \quad [A11]$$

Given the Taylor series expansion, we can approximate this as

$$\begin{aligned}S_{Slc}(t)&\approx\int_x M_{SS}\Big(\alpha(x)\Big)\left(\left(1-2e^{-\frac{t}{T_1}}\right)+\frac{te^{-\frac{t}{T_1}}}{TR}\alpha(x)^2\right)dx\\&=\int_x M_{SS}\Big(\alpha(x)\Big)\left(1-2e^{-\frac{t}{T_1}}\right)dx+\int_x M_{SS}\Big(\alpha(x)\Big)\frac{te^{-\frac{t}{T_1}}}{TR}\alpha(x)^2dx\\&=\int_x M_{SS}\Big(\alpha(x)\Big)\left(1-2e^{-\frac{t}{T_1}}\right)dx+\frac{te^{-\frac{t}{T_1}}}{TR}\int_x M_{SS}\Big(\alpha(x)\Big)\alpha(x)^2dx\\&=\left(\int_x M_{SS}\Big(\alpha(x)\Big)dx\right)\left(\left(1-2e^{-\frac{t}{T_1}}\right)+\frac{te^{-\frac{t}{T_1}}}{TR}\underbrace{\frac{\int_x M_{SS}\Big(\alpha(x)\Big)\alpha(x)^2dx}{\int_x M_{SS}\Big(\alpha(x)\Big)dx}}_{:=\alpha^2_{Slc}}\right)\\&\approx\left(\int_x M_{SS}\Big(\alpha(x)\Big)dx\right)\cdot R(t,\alpha_{Slc})\end{aligned} \quad [A12]$$

where the last line follows the Taylor series approximation.

Given a three-parameter model fit with $f(t;A,B,T_1^*)=A-Be^{-\frac{t}{T_1^*}}$,

$$[\hat{A},\hat{B},\hat{T}_1^*]=\text{argmin}_{A,B,T_1^*}\sum_t|\text{f(t; A, B, T}_1^*)-S_{Slc}(t)|^2. \quad [A11]$$

and assuming that a global minimum exists as per convention, indicating the objective function is locally convex around it, we conclude that

$$\frac{1}{\hat{T}_1^*}\approx\frac{1}{T_1}-\frac{\log\Big(\cos(\alpha_{Slc})\Big)}{TR}\Rightarrow$$

$$T_1\approx\left(\frac{1}{\hat{T}_1^*}+\frac{\log\left(\cos\left(\sqrt{\frac{\int_x M_{SS}\Big(\alpha(x)\Big)\alpha(x)^2dx}{\int_x M_{SS}\Big(\alpha(x)\Big)dx}}\right)\right)}{TR}\right)^{-1} \quad [A13]$$

Numerical simulations were performed to study the accuracy of this slice-profile correction. Details and results are provided in Supporting Figure S2.

Note that Equation [A13] requires the knowledge of T_1 to calculate $M_{ss}(\alpha)$ as given in Equation [A2]. To overcome this circularity, we iteratively calculate T_1 using Equation [A13], initialized with $M_{ss}(\alpha)$, corresponding to the T_1 obtained without slice-profile correction. Numerical simulations were performed to illustrate the convergence of this iterative process and are provided in Supporting Figure S3.

ACKNOWLEDGMENTS

The authors thank Ehsan Sedaghat-Nejad for his valuable help with designing the figures.

REFERENCES

1. Kramer CM. Role of cardiac MR imaging in cardiomyopathies. J Nucl Med 2015;56:39S–45S.
2. von Knobelsdorff-Brenkenhoff F, Schulz-Menger J. Cardiovascular magnetic resonance imaging in ischemic heart disease. J Magn Reson Imaging 2012;36:20–38.
3. van der Wall EE, Vliegen HW, de Roos A, Bruschke AV. Magnetic resonance imaging in coronary artery disease. Circulation 1995;92: 2723–2739.
4. Schelbert EB, Messroghli DR. State of the art: clinical applications of cardiac T1 mapping. Radiology 2016;278:658–676.
5. Jellis CL, Kwon DH. Myocardial T1 mapping: modalities and clinical applications. Cardiovasc Diagn Ther 2014;4:126–137.
6. Ambale-Venkatesh B, Lima JA. Cardiac MRI: a central prognostic tool in myocardial fibrosis. Nat Rev Cardiol 2015;12:18–29.
7. Radenkovic D, Weingartner S, Ricketts L, Moon JC, Captur G. T1 mapping in cardiac MRI. Heart Fail Rev 2017;22:415–430.
8. Look DC, Locker DR. Time saving in measurement of NMR and EPR relaxation times. Rev Sci Instrum 1970;41:250–251.
9. Nacif MS, Turkbey EB, Gai N, Nazarian S, van der Geest RJ, Noureldin RA, Sibley CT, Ugander M, Liu S, Arai AE, Lima JA, Bluemke DA. Myocardial T1 mapping with MRI: comparison of look-locker and MOLLI sequences. J Magn Reson Imaging 2011;34:1367–1373.

10. Messroghli DR, Radjenovic A, Kozerke S, Higgins DM, Sivananthan MU, Ridgway JP. Modified Look-Locker inversion recovery (MOLLI) for high-resolution T1 mapping of the heart. Magn Reson Med 2004; 52:141–146.
11. Kvernby S, Warntjes MJ, Haraldsson H, Carlhall CJ, Engvall J, Ebbers T. Simultaneous three-dimensional myocardial T1 and T2 mapping in one breath hold with 3D-QALAS. J Cardiovasc Magn Reson 2014; 16:102.
12. Mehta BB, Chen X, Bilchick KC, Salerno M, Epstein FH. Accelerated and navigator-gated look-locker imaging for cardiac T1 estimation (ANGIE): development and application to T1 mapping of the right ventricle. Magn Reson Med 2015;73:150–160.
13. Weingartner S, Roujol S, Akcakaya M, Basha TA, Nezafat R. Free-breathing multislice native myocardial T1 mapping using the slice-interleaved T1 (STONE) sequence. Magn Reson Med 2015;74:115–124.
14. Chow K, Flewitt JA, Green JD, Pagano JJ, Friedrich MG, Thompson RB. Saturation recovery single-shot acquisition (SASHA) for myocardial T(1) mapping. Magn Reson Med 2014;71:2082–2095.
15. Higgins DM, Ridgway JP, Radjenovic A, Sivananthan UM, Smith MA. T1 measurement using a short acquisition period for quantitative cardiac applications. Med Phys 2005;32:1738–1746.
16. Weingartner S, Akcakaya M, Basha T, Kissinger KV, Goddu B, Berg S, Manning WJ, Nezafat R. Combined saturation/inversion recovery sequences for improved evaluation of scar and diffuse fibrosis in patients with arrhythmia or heart rate variability. Magn Reson Med 2014;71:1024–1034.
17. Weingartner S, Akcakaya M, Roujol S, Basha T, Tschabrunn C, Berg S, Anter E, Nezafat R. Free-breathing combined three-dimensional phase sensitive late gadolinium enhancement and T1 mapping for myocardial tissue characterization. Magn Reson Med 2015;74:1032–1041.
18. Roujol S, Weingärtner S, Foppa M, Chow K, Kawaji K, Ngo LH, Kellman P, Manning WJ, Thompson RB, Nezafat R. Accuracy, precision, and reproducibility of four T1 mapping sequences: a head-to-head comparison of MOLLI, ShMOLLI, SASHA, and SAPPHIRE. Radiology 2014;272:683–689.
19. Weingartner S, Messner NM, Budjan J, Lossnitzer D, Mattler U, Papavassiliu T, Zollner FG, Schad LR. Myocardial T1-mapping at 3T using saturation-recovery: reference values, precision and comparison with MOLLI. J Cardiovasc Magn Reson 2016;18:84.
20. Teixeira T, Hafyane T, Stikov N, Akdeniz C, Greiser A, Friedrich MG. Comparison of different cardiovascular magnetic resonance sequences for native myocardial T1 mapping at 3T. J Cardiovasc Magn Reson 2016;18:65.
21. Reiter U, Reiter G, Dorr K, Greiser A, Maderthaner R, Fuchsjager M. Normal diastolic and systolic myocardial T1 values at 1.5-T MR imaging: correlations and blood normalization. Radiology 2014;271: 365–372.
22. Ferreira VM, Wijesurendra RS, Liu A, Greiser A, Casadei B, Robson MD, Neubauer S, Piechnik SK. Systolic ShMOLLI myocardial T1-mapping for improved robustness to partial-volume effects and applications in tachyarrhythmias. J Cardiovasc Magn Reson 2015;17:77.
23. Coolen BF, Geelen T, Paulis LE, Nauerth A, Nicolay K, Strijkers GJ. Three-dimensional T1 mapping of the mouse heart using variable flip angle steady-state MR imaging. NMR Biomed 2011;24:154–162.
24. Kellman P, Hansen MS. T1-mapping in the heart: accuracy and precision. J Cardiovasc Magn Reson 2014;16:2.
25. Kellman P, Bandettini WP, Mancini C, Hammer-Hansen S, Hansen MS, Arai AE. Characterization of myocardial T1-mapping bias caused by intramyocardial fat in inversion recovery and saturation recovery techniques. J Cardiovasc Magn Reson 2015;17:33.
26. Deichmann R, Haase A. Quantification of T1 values by SNAPSHOT-FLASH NMR Imaging. J Magn Reson 1992;96:608–612.
27. Lakkadi N, Rosen M, Bolan PJ. Design of a phantom for multiparametric quantitative MR imaging and spectroscopy. In Proceedings of the 23rd Annual Meeting of the ISMRM, Toronto, Ontario, Canada, 2015. p. 4285.
28. Kellman P, Herzka DA, Hansen MS. Adiabatic inversion pulses for myocardial T1 mapping. Magn Reson Med 2014;71:1428–1434.
29. Weingartner S, Messner NM, Zollner FG, Akcakaya M, Schad LR. Black-blood native T1 mapping: blood signal suppression for reduced partial voluming in the myocardium. Magn Reson Med 2017;78:484–493.
30. Wassmuth R, Prothmann M, Utz W, Dieringer M, von Knobelsdorff-Brenkenhoff F, Greiser A, Schulz-Menger J. Variability and homogeneity of cardiovascular magnetic resonance myocardial T2-mapping in volunteers compared to patients with edema. J Cardiovasc Magn Reson 2013;15:27.
31. Krishnamurthy R, Cheong B, Muthupillai R. Tools for cardiovascular magnetic resonance imaging. Cardiovasc Diagn Ther 2014;4:104–125.
32. Weingartner S, Moeller S, Schmitter S, Auerbach E, Kellman P, Shenoy C, Akcakaya M. Simultaneous multislice imaging for native myocardial T1 mapping: improved spatial coverage in a single breath-hold. Magn Reson Med 2017;78:462–471.
33. Weingärtner S, Zimmer F, Metzger GJ, Ugurbil K, Van de Moortele PF, Akcakaya M. Motion-robust cardiac B1+mapping at 3T using interleaved bloch-siegert shifts. Magn Reson Med 2017;78:670–677.
34. Cunningham CH, Pauly JM, Nayak KS. Saturated double-angle method for rapid B1+mapping. Magn Reson Med 2006;55:1326–1333.
35. Weingartner S, Akcakaya M, Roujol S, Basha T, Stehning C, Kissinger KV, Goddu B, Berg S, Manning WJ, Nezafat R. Free-breathing post-contrast three-dimensional T1 mapping: volumetric assessment of myocardial T1 values. Magn Reson Med 2015;73:214–222.
36. Chow K, Yang Y, Shaw P, Kramer CM, Salerno M. Robust free-breathing SASHA T1 mapping with high-contrast image registration. J Cardiovasc Magn Reson 2016;18:47.
37. Schweser F, Deistung A, Reichenbach JR. Foundations of MRI phase imaging and processing for Quantitative Susceptibility Mapping (QSM). Z Med Phys 2016;26:6–34.
38. Schar M, Vonken EJ, Stuber M. Simultaneous B(0)- and B(1)+-map acquisition for fast localized shim, frequency, and RF power determination in the heart at 3 T. Magn Reson Med 2010;63:419–426.
39. Xue H, Greiser A, Zuehlsdorff S, Jolly MP, Guehring J, Arai AE, Kellman P. Phase-sensitive inversion recovery for myocardial T1 mapping with motion correction and parametric fitting. Magn Reson Med 2013;69:1408–1420.
40. Kim RJ, Wu E, Rafael A, Chen EL, Parker MA, Simonetti O, Klocke FJ, Bonow RO, Judd RM. The use of contrast-enhanced magnetic resonance imaging to identify reversible myocardial dysfunction. New Eng J Med 2000;343:1445–1453.
41. Kellman P, Wilson JR, Xue H, Ugander M, Arai AE. Extracellular volume fraction mapping in the myocardium, part 1: evaluation of an automated method. J Cardiovasc Magn Reson 2012;14:63.
42. Xue H, Shah S, Greiser A, Guetter C, Littmann A, Jolly MP, Arai AE, Zuehlsdorff S, Guehring J, Kellman P. Motion correction for myocardial T1 mapping using image registration with synthetic image estimation. Magn Reson Med 2012;67:1644–1655.
43. Roujol S, Foppa M, Weingartner S, Manning WJ, Nezafat R. Adaptive registration of varying contrast-weighted images for improved tissue characterization (ARCTIC): application to T1 mapping. Magn Reson Med 2015;73:1469–1482.
44. Swoboda PP, McDiarmid AK, Erhayiem B, et al. Effect of cellular and extracellular pathology assessed by T1 mapping on regional contractile function in hypertrophic cardiomyopathy. J Cardiovasc Magn Reson 2017;19:16.
45. Nakamori S, Dohi K, Ishida M, et al. Native T1 mapping and extracellular volume mapping for the assessment of diffuse myocardial fibrosis in dilated cardiomyopathy. JACC Cardiovasc Imaging 2017. doi: 10.1016/j.jcmg.2017.04.006.
46. Reinstadler SJ, Stiermaier T, Liebetrau J, et al. Prognostic significance of remote myocardium alterations assessed by quantitative noncontrast T1 mapping in ST-segment elevation myocardial infarction. JACC Cardiovasc Imaging 2017. doi: 10.1016/j.jcmg.2017.03.015.
47. Vasanji Z, Sigal RJ, Eves ND, Isaac DL, Friedrich MG, Chow K, Thompson RB. Increased left ventricular extracellular volume and enhanced twist function in type 1 diabetic individuals. J Appl Physiol (1985) 2017;123:394–401.
48. Wu LM, An DL, Yao QY, Ou YZ, Lu Q, Jiang M, Xu JR. Hypertrophic cardiomyopathy and left ventricular hypertrophy in hypertensive heart disease with mildly reduced or preserved ejection fraction: insight from altered mechanics and native T1 mapping. Clin Radiol 2017. doi: 10.1016/j.crad.2017.04.019.
49. Cameron D, Vassiliou VS, Higgins DM, Gatehouse PD. Towards accurate and precise T 1 and extracellular volume mapping in the myocardium: a guide to current pitfalls and their solutions. MAGMA 2017. doi: 10.1007/s10334-017-0631-2.

50. Steen M, Weingärtner S, Akcakaya M. Multi-scale locally low-rank noise reduction for high-resolution dynamic quantitative cardiac MRI In Proceedings of the Annual International Conference of the 39th Annual Meeting of the IEEE Engineering in Medicine and Biology Society, JeJu Island, Korea, 2017. p. 837.

SUPPORTING INFORMATION

Additional Supporting Information may be found in the online version of this article.

Fig. S1. Illustration of the second-order approximation to the inversion-recovery signal model, as described in Equation [A10]. **a**: In the top row the signal is plotted against the FA for several inversion times, *t*. Highly nonlinear trends can be observed with nonzero curvature, even for small FAs. In the lower row, the correlation coefficient between the signal and the FA is listed. Consistently low values indicate poor approximation of the signal function for small FAs. **b**: In the top row, the same signal is plotted against the FA, in which the FA axis is now scaled quadratically instead of linear. Good approximation of the signal curve in the small FA regime can now be obtained by a linear function, as indicated with the dashed lines. The lower row lists the correlation coefficients between the signal and the square of the FA, confirming good approximation with the model proposed in Equation [A10].

Fig. S2. Numerical Bloch simulation of a TOPAZ sequence was performed to study the accuracy of the proposed slice-profile correction as explained in the "Methods" section, except no noise was added in this simulation. The simulated T_1 deviation from the ground truth, with and without using the proposed slice-profile correction, at various FAs and slice profiles (bandwidth-time product), are shown above. The TR was fixed to 5 ms for this simulation, and the simulated ground truth T_1 time was 1550 ms. The red circles indicate the actual acquisition parameters from the paper, resulting in a T_1 deviation of 4.3 ms using the proposed correction.

Fig. S3. Difference between slice-profile correction using ground truth T_1 time in the calculation of $M_{SS}(\alpha)$ and using an iteratively estimated T_1, with a varying number of iterations (see Appendix). Simulations were performed with TR = 5 ms, $\alpha = 3^\circ$, and bandwidth-time products (BWT) as listed in the legend. The simulated $T_1 = 1550$ ms.

Fig. S4. All baseline images as acquired in a healthy subject with the proposed TOPAZ T_1 mapping sequence, providing five different inversion times and 12 cardiac phases at 50 ms temporal resolution. All images are displayed with the same window level. Visually high contrast is depicted between the myocardium and the blood pools in the earlier images before the zero crossing, which happens around the time point of one R-R interval after the inversion pulse. Longer inversion times depict higher overall signal and weaker contrast, displaying increased proton density weighting. The corresponding T_1 maps show comparable T_1 times across the cardiac cycle. Visually decreased homogeneity is observed in the later phases, which is in accordance with the decreased dynamic signal range.

Fig. S5. In vivo T_1 and B_1^+ maps acquired jointly in a healthy subject with TOPAZ T_1 mapping, at a temporal resolution of 40 ms. Visually high T_1 map quality with homogeneous signal in the myocardium is observed. Good B_1^+ quality is observed at the earlier heart phases, but is degraded toward the end of the cardiac cycle.

Video SV1. Cardiac phase-resolved myocardial T_1 maps acquired in a healthy subject using TOPAZ T_1 mapping. The dynamic T_1 maps are depicted in a cine view in the form of a video. Average T_1 time and standard deviation within a manually drawn septal ROI are indicated in the color bar.

Video SV2. Cardiac phase-resolved myocardial T_1 maps acquired in a healthy subject using TOPAZ T_1 mapping. The dynamic T_1 maps are depicted in a cine view in the form of a video. Average T_1 time and standard deviation within a manually drawn septal ROI are indicated in the color bar.

Video SV3. Cardiac phase-resolved myocardial T_1 maps acquired in a healthy subject using TOPAZ T_1 mapping. The dynamic T_1 maps are depicted in a cine view in the form of a video. Average T_1 time and standard deviation within a manually drawn septal ROI are indicated in the color bar.